Spatial coherence of interplanetary coronal mass ejection sheaths at 1 AU

Matti Ala-Lahti[1], Julia Ruohotie[1], Simon Good[1], Emilia K. J. Kilpua[1], and Noé Lugaz[2]

[1]Department of Physics, P.O. Box 64, University of Helsinki, Helsinki, Finland
[2]Space Science Center and Department of Physics, University of New Hampshire, Durham, NH, USA

Key Points:

- Spatial coherence length of magnetic field in ICME sheaths is larger than in the solar wind and typically smaller than in ICME ejecta.
- High frequency fluctuations are localized in ICME sheaths.
- Large correlation length for B_y is consistent with field line draping and shock deflection.

Corresponding author: Matti Ala-Lahti, matti.ala-lahti@helsinki.fi

Abstract

The longitudinal spatial coherence near 1 AU of the magnetic field in sheath regions driven by interplanetary coronal mass ejection (ICME) is studied by investigating ACE and *Wind* spacecraft measurements of 29 sheaths. During 2000-2002 *Wind* performed prograde orbits, and the non-radial spacecraft separation varied from 0.001 to 0.012 AU between the studied events. We compare the measurements by computing the Pearson correlation coefficients for the magnetic field magnitude and components, and estimate the magnetic field coherence by evaluating the scale lengths that give the extrapolated distance of zero correlation between the measurements. The correlation is also separately examined for low- and high-pass filtered data. We discover magnetic fields in ICME sheaths have scale lengths that are larger than those reported in the solar wind but that, in general, are smaller than the ones of the ICME ejecta. Our results imply that magnetic fields in the sheath are more coherently structured and well correlated compared to the solar wind. The largest sheath coherence is reported in the GSE y-direction that has the scale length of 0.149 AU while the lengths for B_x, B_z, and $|B|$ vary between 0.024 and 0.035 AU. The same sheath magnitude ordering of scale lengths also apply for the low-pass filtered magnetic field data. We discuss field line draping and the alignment of pre-existing discontinuities by the shock passage giving reasoning for observed results.

1 Introduction

Interplanetary coronal mass ejections (ICMEs), originating from drastic eruptions at the Sun, often form complexes consisting of a leading shock, turbulent sheath, and magnetic ejecta itself (Burlaga et al., 1981, 1982; Tsurutani et al., 2003; Kilpua, Koskinen, & Pulkkinen, 2017). While ICME ejecta act as extreme drivers of geoeffectivity at the Earth (e.g., Wilson, 1987; Tsurutani et al., 1988; G. Zhang & Burlaga, 1988; Koskinen & Huttunen, 2006; J. Zhang et al., 2007) and preceding shocks interact with the entire magnetosphere (Samsonov et al., 2007), recent studies (e.g., Yermolaev et al., 2012; Lugaz et al., 2016; Myllys et al., 2016; Kilpua, Balogh, et al., 2017) have highlighted the strong solar wind-magnetosphere coupling that occurs during the passage of the sheath region. A significant fraction of space weather storms are, in fact, partly or entirely induced by the sheath region (Huttunen & Koskinen, 2004).

In addition to extended periods of southward magnetic field, geoeffectiveness of the sheath is affected by the presence of discontinuities, turbulence and waves (Tsurutani et al., 1988). Kilpua et al. (2019) reported both the vicinity of the shock and ejecta leading edge to be the most geoeffective regions within ICME sheaths, regions that are also associated with high magnetic field magnitudes and fluctuation amplitudes, and out-of-ecliptic fields. High magnetic field magnitude (Owens et al., 2005; Kilpua et al., 2019; Janvier et al., 2019) and higher power of magnetic fluctuations (Kilpua et al., 2013; Moissard et al., 2019) are also observed to correlate with the speed of the ejecta (Owens et al., 2005; Kilpua et al., 2019).

Sheath regions of ICMEs are characterized by field line draping (Gosling & McComas, 1987) and plasma depletion (Liu et al., 2006). In addition, different wave structures often appear in ICME-driven sheath regions. Mirror mode (Ala-Lahti et al., 2018) and Alfvén ion cyclotron (Ala-Lahti et al., 2019) waves occur frequently in sheaths, especially near the preceding shock. The existence of both large- and small-scale sheath structures stem from the inhomogeneous solar wind plasma and magnetic field encountered by the ICME travelling away from the Sun. The shock aligns and compresses pre-existing solar wind discontinuities (Neugebauer et al., 1993; Kataoka et al., 2005) and provides a source of free energy for the excitation of plasma waves in the sheath. Since ICMEs typically expand strongly in the inner heliosphere, the plasma tends to pile up at its leading edge due to decreased deflection (Siscoe & Odstrcil, 2008).

Previous studies have often used either single-point observations (Owens et al., 2005) or compared observations within the sheath at different heliocentric distances (Good et al., 2020; Lugaz et al., 2020; Salman et al., 2020). There is not, however, an understanding of the extent to which different structures and their generation mechanisms are localized in the sheath. This knowledge of the longitudinal extent of magnetic fluctuations is highly important for understanding the formation and evolution of the sheaths and for the capability to predict and estimate their geoeffectiveness (Manchester et al., 2005; Kay et al., 2020). Recent studies (e.g., Owens et al., 2017; Lugaz et al., 2018) have even questioned the coherence of ICME ejecta, which are more organized structures than sheaths. Lugaz et al. (2018) studied 35 ICME ejecta using magnetic field measurements from longitudinally separated spacecraft in the solar wind close to the Earth. They found that the correlation in the magnetic field magnitude and components decrease surprisingly quickly with the increasing spacecraft separation and reported the scale length of longitudinal magnetic coherence to vary between 0.06–0.26 AU.

In this study, we perform the first comprehensive analysis on the longitudinal spatial coherence of magnetic field in ICME sheath regions. We use the measurements of ACE and *Wind* spacecraft at 1 AU to perform a correlation analysis. We apply the results to estimate the maximum spatial extent of magnetic structures within ICME sheaths and discuss the dependence on fluctuation frequency. In the end, we discuss possible reasoning for the results, illustrate the scale of longitudinal coherence compared to the near-Earth space and put across the importance of multi-spacecraft studies positioned in the solar wind.

2 Data and Methods

We construct our analysis from ICMEs reported by Lugaz et al. (2018), whose event list is a suitable collection of events observed at 1 AU by both ACE and *Wind* spacecraft. The events were predominantly observed between September, 2000 and July, 2002 when the separation of the spacecraft in the Geocentric Solar Ecliptic (GSE) y-direction grew to 0.014 AU (320 R_E; see Lugaz et al., 2018, *Introduction*). The time interval was close to the maximum of solar cycle 23. This time period has previously been utilized in investigations of longitudinal features of the solar wind and its turbulence (King & Papitashvili, 2005; Ogilvie et al., 2007; Wicks et al., 2009) and interplanetary shocks (Koval & Szabo, 2010).

Of the 35 events studied by Lugaz et al. (2018), we omit a few events that lacked sheaths or that had ambiguous sheath boundaries. Our final list includes 29 ICME-driven sheath regions in total. The list of studied events is given in the supplementary. Sheath boundaries are defined by the signatures of a fast forward shock and magnetic ejecta, and they are primarily taken from Palmerio et al. (2016) and complemented with some events from the Nieves-Chinchilla et al. (2018) *Wind* ICME catalogue. Only the boundaries of the sheath on 31 March 2001 are defined without the information of the aforementioned lists.

We estimate the spatial coherence by computing the Pearson correlation coefficients (σ_P) between the magnetic field measurements of the two spacecraft and compare them to the non-radial spacecraft separation, i.e., the separation in the y- and z-directions in the GSE coordinates. In addition to calculating the correlation of the individual magnetic field magnitude and its components in the GSE coordinates, we measure an overall Pearson correlation by applying the averaging estimator of correlation coefficients proposed by Olkin and Pratt (1958) for the σ_P values of the magnitude and components. We use σ_{tot} when referring to this total correlation defined as

$$\sigma_{tot} = \frac{\sum_{i=1}^{4}(n_i - 1)}{\sum_{i=1}^{4}(n_i - 4)} \left[\sigma_{P,i} + \frac{\sigma_{P,i}(1 - \sigma_{P,i}^2)}{2(n_i - 3)} \right], \quad (1)$$

where i refers to the magnetic field (component), $\sigma_{P,i}$ is corresponding Pearson correlation coefficient, and n is the size of a sample (Alexander, 1990).

We shift *Wind* data and maximize cross-correlation of σ_{tot} for an individual event. Correlations are also given for the shift that aligns the beginning of a sheath, defined by a fast forward shock, in the spacecraft measurements. We refer to this from now on as *shock alignment (SA)*. We note, however, that from now on *Wind* data has been shifted according to the maximized σ_{tot} if not mentioned otherwise. We test the procedure calculating correlation coefficients for 1-min time-averaged data (i.e., data time-averaged over successive 1-min intervals), and for time averages ranging between 5 and 20 min in increments of 5 min. The typical radial length of a 5–20 min plasma stream in a sheath is 0.001–0.004 AU (Kilpua et al., 2019) and sets an upper limit for the non-radial length of the stream, assuming that the radial flow speed is equal to or in excess of the non-radial speed. Thus, the non-radial length of a 5–20 min plasma stream is smaller than the typical non-radial spacecraft separation, which had a 20% quantile of 0.004 AU, implying the spacecraft did not observe the same stream and its embedded magnetic field.

The average correlations of all events are shown separately for the field magnitude and components in Fig. 1a. Figure 1a also plots the total correlation, σ_{tot}, averaged over all studied events (blue curve) with the lower and upper bounds for a 95% confidence interval (black dots) as a function of the length of the data averaging window. The values of σ_P of magnetic field magnitude and components (colored circles), and the total correlation according to the shock alignment (yellow curve) are also shown. There is a general trend of increasing correlations as a function of the length of an averaging window (W).

In addition, Fig. 1a plots the average number of data points within an ICME sheath (N, red curve), with error bars indicating the sizes of the smallest and largest samples. The dashed red line $N = 25$ indicates the recommended lower limit for the Pearson correlation estimation (David et al., 1938), by reason of which we choose 5 min averaging window length for determining correlation scale lengths in Section 3. P-values (or values above which a null hypothesis exists) are given in Fig. 1a for $W = 5$ min, and are below the nominal significance level (0.05) indicating significant correlations.

Figure 1b shows the average correlations for $W = 5$ min as a function of time lag, i.e., how much *Wind* data is shifted to align the spacecraft measurements, with respect to the shift giving the highest possible correlation of σ_{tot} for a single event. Thus, the total correlation of an individual event and also the averaged one peak at zero time lag by definition. The correlations of the magnitude and all components (dashed), moreover, are peaked at zero time lag but the two extremes of $\sigma_{tot,SA}$ are associated with the time lags of $\sim$3 and $\sim$9 min. This difference can be due to a possible variation in estimation of a shock transition or alternatively, measurements might include coherent patterns having a lag that deviates from the one giving the shock alignment.

The double-peaked distribution may also result from minor differences in the sheath passage duration at the two spacecraft. The peak at $\sim$9 min time lag corresponds to the shock alignment shift. Given that ACE observed the sheath earlier than *Wind* in 28 of 29 cases, the peak at $\sim$3 time lag implies alignment of the sheath rear. Thus, together the curves of σ_{tot} and the one for shock alignment hint the importance of the sheath trailing portion in the correlation. The sheath may evolve and expand during the propagation between ACE and *Wind*, which typically took $\sim$30–60 min during the prograde orbit of *Wind*. Then the sheath rear can be expected to be older, and thus more coherent, than the sheath front, which is exposed to new material accumulated during sheath propagation. We note that all correlations drop quickly as a function of increasing and decreasing time lag.

We conclude this section by showing an example event observed by the spacecraft on 15 May 2005 in Fig. 2. For this event, the non-radial spacecraft separation was 0.0036 AU and the shift of *Wind* data is the same for both maximizing σ_{tot} and shock alignment. Correlation coefficients of magnetic field measurements are given for 1 and 5 min averaged data to illustrate how averaging smooths fluctuations. Although the correlation is quite high for the magnetic field magnitude ($\sigma_P = 0.9$), it varies between the magnetic field components

and is considerably lower in the y-direction ($\sigma_P = 0.4$). B_y for this example event shows some anti-correlated features (e.g., at ∼3:00) that would become well correlated (and hence give an increased σ_P of B_y) for a different time shift. However, time lags that increase correlation for certain features could reduce correlation of other features. We emphasize that the shifting in our study is defined according to the maximized σ_{tot} that also maximizes σ_P of each component over the average of all studied events, as was seen in Fig. 1b.

3 Results

We here report and discuss the Pearson correlation coefficients of the magnetic field measurements as a function of the non-radial spacecraft separation, which varied between 0.001 and 0.012 AU. The GSE y-component of the separation was $> 97\%$ of the absolute separation distance in all cases. The results for all studied ICME-sheath events are shown in Fig. 3.

In addition, we estimate the extent of spatial coherence of the magnetic field in the non-radial direction by applying the least-squares linear fitting for the data shown in Fig. 3 and finally extrapolating the fittings until zero correlation is achieved. Similar to Lugaz et al. (2018), we refer to this extrapolated distance with zero correlation as the scale length of the magnetic field (component). The linear fittings and the corresponding scale lengths are given in Fig. 3 and Table 1, respectively. In Table 1 we also list the scale lengths of an ICME reported by Lugaz et al. (2018) for 30 min averaging.

A decreasing trend in Pearson correlation coefficients for $|B|$, B_x, B_z with increasing spacecraft separation is deducible in Fig. 3. The scale lengths of ICME sheaths for these magnetic field parameters are lower than for the ICME ejecta being 12, 37, and 57% (*SA:* 11, 31, and 34%) of the ones for the ejecta (see Table 1), respectively. We note the decreasing trend also applies for σ_{tot}. Compared to the aforementioned scale lengths, the length is discernibly large for B_y. It is 0.149 ± 0.035 AU being 159% (*SA:* 0.042 ± 0.002 AU, 45%) of that for ejecta.

Furthermore, following Lugaz et al. (2018), we separate the sheaths into two groups according to the non-radial spacecraft separation being less than or larger than 0.008 AU (sample sizes 14 and 15, respectively) and compute the p-values implying the probability that the means of two samples are the same (Welch, 1938). While the p-values for $|B|$, B_x, B_z and σ_{tot} vary between 0.008 (B_x) and 0.069 ($|B|$), the value of 0.938 for B_y indicates that the descending trend in Fig. 3c is not statistically significant (p-values for *SA:* vary between 0.002 and 0.041 for σ_{tot} and B_x, respectively, and B_y has the value of 0.129). This implies the estimated scale length for B_y can be even larger than reported above.

Similarly to Lugaz et al. (2018), we compute correlation coefficients between the correlations of the magnetic field measurements and the non-radial spacecraft separation and between the correlations and shock parameters, which are taken from the Heliospheric Shock Database (see Kilpua et al., 2015) for both spacecraft. We consider here the angle in which the IMF field crossed the shock from upstream (θ_{Bn} i.e., the shock angle), the angle of the shock normal and radial direction (θ_{nr}), shock speed (V_{sh}) and shock Alfvén Mach number (M_A). The results are given in Table 2.

We find the following correlations for the non-radial separation (SA), given in ascending order: σ_{tot}: -0.57 (-0.62), B_z: -0.55 (-0.55), B_x: -0.47 (-0.56), $|B|$: -0.42 (-0.40), and B_y: -0.11 (-0.27). The absolute values of these correlations have a 25% quantile of 0.34 (SA: 0.37). The correlation coefficients for shock parameters are typically smaller. Coefficients for shock parameters defined from *Wind*/ACE measurements have a 75% quantile of 0.27/0.28 (0.26/0.28) for their absolute values. Coefficients of a given magnetic field and shock parameter vary significantly between both the alignments and spacecraft measurements used to define the parameters. Only a few coefficients for shock parameters have $|\sigma_P| > 0.40$.

Finally, we study how correlation depends on the frequency of magnetic fluctuations. We plot in Fig. 4a the averaged correlation similarly as in Fig. 1 for low- and high-pass filtered data as a function of cutoff frequency. We also plot the correlation for the root-mean-square of the magnetic field vector (B_{RMS}), which indicates the level of fluctuations and is enhanced in geoeffective sheaths (Kilpua et al., 2019), as a function of the inverse of the root-mean-square time window.

The total correlation, σ_{tot} is shown as a function of cutoff frequency and non-radial spacecraft separation in Fig. 4b and c. Fig. 4b and c also plot the contours of $\sigma_{tot} = 0.8$ and 0.9, and $\sigma_{tot} = 0.3$ and 0.5, respectively. For comparison, these contours are also given for B_y. Figure 4c shows the corresponding graph of B_{RMS} with the contours of $\sigma_P = 0.3$ and 0.5.

For the low-pass filtered magnetic field data (Fig. 4a), the correlations show a coincident pattern to the results given in Fig. 3 and Table 1 throughout the entire cutoff frequency variation. The correlation is consistently highest (lowest) for B_y (B_x). Moreover, correlations for the high-pass filtered data decrease quickly towards zero as a function of cutoff frequency, being below 0.05 for frequencies above $1.5 \cdot 10^{-3}$ Hz, which, together with decreasing B_{RMS}, imply the presence of localized higher frequency fluctuations that are spatially limited in extent. The notable differences in the correlations of different magnetic field components are, however, less distinguished for the high-pass filtered data than in the case of the low-pass filtering (see for example B_y and B_z). Interestingly, the correlation of the high-pass filtered B_z data is slightly higher than the one of B_y for the frequency (f) interval of $2 \cdot 10^{-4} < f < 2 \cdot 10^{-2}$.

High correlation is associated with low frequencies and small spacecraft separations in Fig. 4b, c and d. Although a given correlation extends to higher frequencies the smaller the spacecraft separation is, as is implied by the contours, the graphs show that lower correlation for higher cutoff frequencies in Fig. 4a is not dominated by just either events having small or large spacecraft separation. For example, for the high-pass filtered data, low correlation ($\sim$ 0) occupies a substantial portion of the whole frequency space for all spacecraft separations. The contours of B_y in Fig. 4c do not either bound the whole frequency space, although they mainly extend to higher frequencies than the ones of σ_{tot}.

Table 1. Scale lengths and their standard deviations of magnetic field magnitude and its components in ICME sheaths. Values are given for both alignments, maximizing σ_{tot} and aligning the beginning of a sheath, and also for total Pearson correlation of magnetic field measurements (σ_{tot}; the bottom row). The standard deviations are computed by using 1, 5, and 10 min data averaging windows. For comparison, we list the values of ICMEs given by Lugaz et al. (2018) for 30 min averaging.

Magnetic Field Parameter	Scale Length [AU]		
	Maximized σ_{tot}	*SA*	ICMEs
$\|B\|$	0.030±0.001	0.028±0.001	0.260
B_x	0.024±0.001	0.020±0.001	0.065
B_y	0.149±0.035	0.042±0.002	0.094
B_z	0.035±0.003	0.021±0.001	0.061
σ_{tot}	0.035±0.002	0.025±0.001	

Table 2. The correlation coefficients between the correlations of the magnetic field measurements and the non-radial spacecraft separation or shock parameters. The values in brackets are for *SA*. The correlations are given for both shock parameters defined by ACE and *Wind* spacecraft measurements.

Magnetic Field Parameter	σ_P with Non-Radial Separation	σ_P with Shock Parameter				
			θ_{Bn}	θ_{nr}	V_{sh}	M_A
$\|B\|$	-0.42 (-0.40)	*Wind*	0.13 (-0.08)	-0.25 (-0.45)	-0.29 (-0.28)	-0.01 (0.03)
		ACE	0.31 (0.37)	0.08 (-0.03)	-0.45 (-0.56)	-0.11 (-0.19)
Bx	-0.47 (-0.56)	*Wind*	-0.09 (-0.11)	-0.26 (-0.12)	-0.24 (-0.17)	-0.34 (-0.26)
		ACE	0.11 (0.02)	0.09 (0.09)	-0.06 (0.01)	-0.43 (-0.022)
By	-0.11 (-0.27)	*Wind*	-0.13 (-0.34)	-0.01 (-0.25)	-0.09 (0.15)	-0.03 (0.03)
		ACE	0.11 (0.17)	0.19 (-0.14)	-0.13 (0.01)	-0.16 (-0.16)
Bz	-0.55 (-0.55)	*Wind*	0.30 (0.16)	0.03 (-0.17)	-0.28 (-0.17)	-0.17 (-0.12)
		ACE	0.11 (0.42)	0.44 (0.29)	-0.16 (-0.17)	-0.07 (-0.14)
σ_{tot}	-0.57 (-0.62)	*Wind*	0.07 (-0.11)	-0.21 (-0.33)	-0.31 (-0.16)	-0.20 (-0.10)
		ACE	0.23 (0.34)	0.23 (0.08)	-0.28 (-0.26)	-0.27 (-0.23)

4 Discussion and Conclusions

We have performed the first statistical analysis of the longitudinal spatial coherence of the magnetic fields in ICME sheaths. Measurements within 29 ICME-driven sheath regions made by ACE and *Wind* spacecraft at 1 AU have been analyzed. The study has discovered that sheaths, typically characterized by large amplitude magnetic field variations, are less coherent than ICME ejecta, which often exhibit a continuously changing magnetic field direction and low magnetic variability. The estimated scale lengths indicating the zero correlation between the measurements at two spacecraft vary between 0.024 and 0.149 AU and are typically clearly smaller for the sheath than the corresponding values reported for the ICME ejecta by Lugaz et al. (2018) (0.061 - 0.260 AU). The comparable scale lengths for the solar wind, on the other hand, vary from 0.004 to 0.025 AU (Richardson & Paularena, 2001; Matthaeus et al., 2005; Wicks et al., 2009). Thus, our results for sheaths settle in between the longitudinal scales of the solar wind and ICME ejecta and suggest that magnetic fields in the sheath are more coherently structured and well correlated in comparison to the solar wind. Interestingly, we discovered a considerably large scale length of B_y, and our data sample does not rule out the possibility of B_y having even larger scale length. We also observe relatively large differences between the scale lengths of magnetic field components for the ICME sheath. Moreover, the differences in correlation are more distinct for the low-pass than high-pass filtered data, and the results further shows (Fig. 4a) that high-frequency fluctuations ($>\sim 10^{-3}$ Hz) are not correlated for the average spacecraft separation analyzed. However, as lower frequency, larger scale fluctuations are gradually added to the correlated time series (i.e., as high-pass cutoff frequency reduces), correlation rises. This rise is more gradual for B_x. Physical processes reported in the context of ICME sheaths are next discussed to analyze the results.

As discussed in the introduction, ICME sheaths are complex heliospheric structures where on-going processes form and generate both large- and small-scale structures. Due to magnetic field line draping around the ICME ejecta, strong out-of-ecliptic fields can occur in the ICME sheath (Gosling & McComas, 1987). The draping pattern is affected, for example, by the size and shape of the ejecta and the direction of the interplanetary magnetic field (IMF). However, in a theoretical case, in which we are only concerned with the ecliptic plane and assume that the IMF settles in the angle of 45° at 1 AU according to the Parker spiral and that no erosion of the ejecta is happening, the ejecta acts as a magnetic obstacle in the radial direction. As a consequence, the plasma is deflecting around the ejecta and the draping IMF should increase from the Parker spiral angle of 45° as a result of an increasing y-component. Magnetic field rotated parallel to the y-axis due to the draping would then have a large-scale consistency of B_y. In a correlation coefficient analysis, this would be seen as a high correlation that is dominated by the large-scale structure, rather than small fluctuations. Because of the reduced large-scale x-component, any local, perpendicular fluctuations are significant deviations from the mean field and lead to a low correlation of B_x. The more gradual rise of B_x in Fig. 4a with reducing cutoff frequency is also explained by this typically less large-scale variation in B_x.

To investigate further deviations from the nominal Parker spiral, we have computed in Fig. 5a the absolute averages of IMF angles (longitude and latitude in the GSE) as a function of the fractional distance in the sheath from the ICME shock to the ejecta leading edge. The azimuthal component (ϕ, solid lines) increases strongly from the solar wind to the sheath and deviates notably from the Parker spiral value of 45° during the whole sheath. The trend, however, is decreasing towards the ICME leading edge which contradicts with the simple concept of field line draping along the East-West direction (i.e., normal to the ICME propagation direction) On the other hand, similarly as was described above for the ecliptic plane, the draping can lead to out-of-ecliptic fields. In Fig. 5a, in the trailing part of the ICME sheath the elevation (θ, dashed lines) increases indicating the enhancement of out-of-ecliptic fields. This increase is possible due to a theoretical draping pattern in which B_x and field magnitude stay constant and the increase of B_z happens at the expense of

decreasing B_y. In that case, field vectors in a unit sphere would be limited to the perimeter of a cone with its axis centered on the x-axis. This scenario is compared to our observations by taking an observational value at the middle of the sheath ($\phi = 60°$, $\theta = 33°$; see Fig. 5a) from which the angles are computed along curves having a constant B_x and $|B|$ until a limiting observational boundary point of (56°, 37°) at the back of the sheath is reached. In Fig. 5a, this scenario is shown by the cyan blue curves which both are within the given error bars, indicating consistency with field line draping despite the decreasing ϕ angle. This description of field line draping, that has a consistency with the direct observations, is illustrated in Fig. 5b for an ICME sheath region driven by a flux rope that is oriented with a low inclination along the east-west line. This is a common rope orientation at 1 AU (Lepping et al., 2006; Good et al., 2019). The figure depicts the ideal draping that generates out-of-ecliptic fields with constant $|B|$ and B_x. Draping patterns can in reality differ from this, being dependent for example on whether the field is draped at the sheath nose or flanks (e.g., Manchester et al., 2005), and on the orientation and shape of the ejecta (e.g., Gosling & McComas, 1987), since the magnetic field drapes tangentially to the local leading surface of the ejecta (Jones et al., 2002). Out-of-ecliptic fields due to draping presumably diminish, for example, when ejecta is oriented north or south, reasoning the intuitive implicit assumption of low ejecta inclination in Fig. 5b.

The deviation from the Parker spiral was already observed by Farrugia et al. (1990), who further suggested that the draping influences the forming of planar magnetic structures (PMSs; Nakagawa et al., 1989) within ICME sheaths. Later Neugebauer et al. (1993) reported the draping as one of the leading causes of PMSs (see also Jones & Balogh, 2000).

Neugebauer et al. (1993) also discussed how pre-existing IMF discontinuities are amplified at the shock crossing and become more aligned with the surface of the shock. PMSs, indeed, also tend to occur downstream of the interplanetary shock preceding the ICME sheath (Kataoka et al., 2005; Palmerio et al., 2016). We observe that for the sheaths considered in this study, the shock normals were close to radial ($\langle\theta_{nr}\rangle = 27° \pm 3°$). This is analogous with the aforementioned scenario of the draping in which perpendicular fluctuations cause a lower coherence in B_x. However, we found weak or no correlation between magnetic field measurements and different shock parameters.

As the low pass filtered magnetic field data also hints that there is a coherent embedded global magnetic field in the ICME sheath (Fig. 4), we conclude that extensive physical mechanisms, such as the field line draping around the ICME ejecta, are plausible explanations for the observed differences in the scale lengths between the magnetic field components. Analysis of our results suggests that field alignments in the ICME sheaths are oblique to the radial direction, and we noted that the maximized total correlation has a displacement from the time lag giving the shock alignment (Fig. 1b). Possible variations in defining the shock transition could cause this. Another possibility is that alignments formed in the draping of the magnetic field are aligned to the surface of the ICME leading edge and not the shock plane (Kataoka et al., 2005). Fixed sheets of magnetic field direction are then measured by the spacecraft with a lag that differs from the lag of aligning the shock boundaries, which further implies the plausible importance of the draping in explaining the presented observations. Our observation of the double-peaked distribution in Fig. 1b coincides with this discussion.

In this study, we have discovered that magnetic fields in the ICME sheath are more coherent than what they are in the solar wind. To illustrate this, we sketch in Fig. 6 an ICME complex in Earth centered interplanetary space and depict the extent of estimated scale lengths and how they compare to the scale lengths observed in the solar wind and ICME ejecta. The figure also illustrates how the interaction of the ICME sheath with the Earth's magnetosphere might vary depending on the location of the sheath passage. The scale lengths are simply exemplified in the y-direction, and the near-Earth space with magnetosphere boundaries is shown in the zoomed box in the figure.

As is depicted in the figure, an ICME complex is massive at 1 AU compared to the magnetosphere of the Earth. Similar non-radial extent of an ICME is reported in simulations (e.g., Riley & Crooker, 2004; Pomoell & Poedts, 2018). Although also the scale lengths are larger than the longitudinal range of the bow shock ($\sim$0.003 AU), their width is substantially smaller than the non-radial diameter of the ICME sheath.

The draping causing out-of-ecliptic magnetic fields associated with preceding Parker spiral orientation of the IMF results in east-west asymmetry in the geoeffectiveness of the ICME sheath (Siscoe et al., 2007). In addition, our results together with the high fluctuation levels in the sheath (Kilpua et al., 2013, 2019; Moissard et al., 2019) raise a question of the occurrence of periods of geoeffective magnetic fields in ICME sheaths that have limited non-radial extent. From this perspective, the nature of the interactions with the magnetosphere would depend on the fine structure of the ICME sheath and not just on the aforementioned more global east-west asymmetry between the sheath flanks. The comparatively higher coherence of B_z (Fig. 4a) for the high-pass filtered magnetic field indeed implies that these local out-of-ecliptic field periods could occur in the interplanetary magnetic field in the sheath. Moreover, southward fields enhanced in the ICME sheath due to compression of pre-existing fields in the shock crossing are often associated with high dynamic pressure, which together cause a particular strong driver of geomagnetic activity at the Earth (Lugaz et al. (2016); Kilpua, Balogh, et al. (2017); see also Lugaz et al. (2015)). Comprehensive research of the evolution of these fields and their possible localness would lead to more accurate specification of the role the ICME sheath has in driving space weather at the Earth. Thus, further multi-scale studies of ICME sheaths, enabled by dedicated multi-spacecraft missions, would improve our understanding of and ability to predict near-Earth space dynamics during the passage of the ICME complex.

Acknowledgments

Data used in this study are available at the NASA Goddard Space Flight Center Coordinated Data Analysis Web (CDAWeb, http://cdaweb.gsfc.nasa.gov/). The investigated magnetic field data is measured by ACE and Wind Magnetic Fields Investigation instruments. The ACE and Wind data sources and their documentation are given by California Institute of Technology (http://www.srl.caltech.edu/ACE/) and NASA (https://wind.nasa.gov/data.php). Shock parameters are provided by the Heliospheric Shock Database, generated and maintained at the University of Helsinki (http://ipshocks.fi/database). Furthermore, a file listing the studied ICME sheaths and the data of Fig. 3 is given. We thank the NASA Goddard Space Flight Center for providing data on CDAWeb. M. A.-L., E. K. and S. G. acknowledge The Finnish Centre of Excellence in Research of Sustainable Space, funded through the Academy of Finland Grant 312351 and Academy of Finland Project 310445 (SMASH). This project has received funding from the European Research Council (ERC) under the European Union's Horizon 2020 research and innovation program (Grant Agreement 724391, SolMAG). NL acknowledges NASA grants 80NSSC20K0700 and 80NSSC17K0009. The authors declare that they have no conflict of interest.

References

Ala-Lahti, M., Kilpua, E. K. J., Dimmock, A. P., Osmane, A., Pulkkinen, T., & Souček, J. (2018, May). Statistical analysis of mirror mode waves in sheath regions driven by interplanetary coronal mass ejection. *Annales Geophysicae*, *36*(3), 793-808. doi: 10.5194/angeo-36-793-2018

Ala-Lahti, M., Kilpua, E. K. J., Souček, J., Pulkkinen, T. I., & Dimmock, A. P. (2019, Jun). Alfvén Ion Cyclotron Waves in Sheath Regions Driven by Interplanetary Coronal Mass Ejections. *Journal of Geophysical Research (Space Physics)*, *124*(6), 3893-3909. doi: 10.1029/2019JA026579

Alexander, R. A. (1990). A note on averaging correlations. *Bulletin of the Psychonomic Society*, *28*(4), 335–336. doi: 10.3758/BF03334037

Burlaga, L. F., Klein, L., Sheeley, J., N. R., Michels, D. J., Howard, R. A., Koomen, M. J., ... Rosenbauer, H. (1982, Dec). A magnetic cloud and a coronal mass ejection. *Geophysical Research Letters*, *9*(12), 1317-1320. doi: 10.1029/GL009i012p01317

Burlaga, L. F., Sittler, E., Mariani, F., & Schwenn, R. (1981, Aug). Magnetic loop behind an interplanetary shock: Voyager, Helios, and IMP 8 observations. *Journal of Geophysical Research*, *86*(A8), 6673-6684. doi: 10.1029/JA086iA08p06673

David, F. N., et al. (1938). Tables of the ordinates and probability integral of the distribution of the correlation in small samples. *Cambridge: Cambridge University Press*.

Farrugia, C. J., Dunlop, M. W., Geurts, F., Balogh, A., Southwood, D. J., Bryant, D. A., ... Etemadi, A. (1990, Jul). An interplanetary planar magnetic structure oriented at a large ($\sim$ 80 deg) angle to the Parker spiral. *Geophysical Research Letters*, *17*(8), 1025-1028. doi: 10.1029/GL017i008p01025

Good, S. W., Ala-Lahti, M., Palmerio, E., Kilpua, E. K. J., & Osmane, A. (2020, April). Radial Evolution of Magnetic Field Fluctuations in an Interplanetary Coronal Mass Ejection Sheath. *The Astrophysical Journal*, *893*(2), 110. doi: 10.3847/1538-4357/ab7fa2

Good, S. W., Kilpua, E. K. J., LaMoury, A. T., Forsyth, R. J., Eastwood, J. P., & Möstl, C. (2019, Jul). Self-Similarity of ICME Flux Ropes: Observations by Radially Aligned Spacecraft in the Inner Heliosphere. *Journal of Geophysical Research (Space Physics)*, *124*(7), 4960-4982. doi: 10.1029/2019JA026475

Gosling, J. T., & McComas, D. J. (1987, Apr). Field line draping about fast coronal mass ejecta: A source of strong out-of-the-ecliptic interplanetary magnetic fields. *Geophysical Research Letters*, *14*(4), 355-358. doi: 10.1029/GL014i004p00355

Huttunen, K., & Koskinen, H. (2004, May). Importance of post-shock streams and sheath region as drivers of intense magnetospheric storms and high-latitude activity. *Annales Geophysicae*, *22*(5), 1729-1738. doi: 10.5194/angeo-22-1729-2004

Janvier, M., Winslow, R. M., Good, S., Bonhomme, E., Démoulin, P., Dasso, S., ... Boakes, P. D. (2019, Feb). Generic Magnetic Field Intensity Profiles of Interplanetary Coronal Mass Ejections at Mercury, Venus, and Earth From Superposed Epoch Analyses. *Journal of Geophysical Research (Space Physics)*, *124*, 812-836. doi: 10.1029/2018JA025949

Jones, G. H., & Balogh, A. (2000, Jun). Context and heliographic dependence of heliospheric planar magnetic structures. *Journal of Geophysical Research*, *105*(A6), 12713-12724. doi: 10.1029/2000JA900003

Jones, G. H., Rees, A., Balogh, A., & Forsyth, R. J. (2002, June). The draping of heliospheric magnetic fields upstream of coronal mass ejecta. *Geophysical Research Letters*, *29*(11), 1520. doi: 10.1029/2001GL014110

Kataoka, R., Watari, S., Shimada, N., Shimazu, H., & Marubashi, K. (2005, Jun). Downstream structures of interplanetary fast shocks associated with coronal mass ejections. *Geophysical Research Letters*, *32*(12), L12103. doi: 10.1029/2005GL022777

Kay, C., Nieves-Chinchilla, T., & Jian, L. K. (2020, Feb). FIDO-SIT: The First Forward Model for the In Situ Magnetic Field of CME-Driven Sheaths. *Journal of Geophysical Research (Space Physics)*, *125*(2), e27423. doi: 10.1029/2019JA027423

Kilpua, E. K. J., Balogh, A., von Steiger, R., & Liu, Y. D. (2017, Nov). Geoeffective Properties of Solar Transients and Stream Interaction Regions. *Space Sci. Rev.*, *212*, 1271-1314. doi: 10.1007/s11214-017-0411-3

Kilpua, E. K. J., Fontaine, D., Moissard, C., Ala-Lahti, M., Palmerio, E., Yordanova, E., ... Turc, L. (2019, Aug). Solar Wind Properties and Geospace Impact of Coronal Mass Ejection-Driven Sheath Regions: Variation and Driver Dependence. *Space Weather*, *17*(8), 1257-1280. doi: 10.1029/2019SW002217

Kilpua, E. K. J., Hietala, H., Koskinen, H. E. J., Fontaine, D., & Turc, L. (2013, Sep). Magnetic field and dynamic pressure ULF fluctuations in coronal-mass-ejection-driven sheath regions. *Annales Geophysicae*, *31*(9), 1559-1567. doi: 10.5194/angeo-31-1559-2013

Kilpua, E. K. J., Koskinen, H. E. J., & Pulkkinen, T. I. (2017, Nov). Coronal mass ejections and their sheath regions in interplanetary space. *Living Reviews in Solar Physics*, *14*(1), 5. doi: 10.1007/s41116-017-0009-6

Kilpua, E. K. J., Lumme, E., Andreeova, K., Isavnin, A., & Koskinen, H. E. J. (2015, Jun). Properties and drivers of fast interplanetary shocks near the orbit of the Earth (1995-2013). *Journal of Geophysical Research (Space Physics)*, *120*(6), 4112-4125. doi: 10.1002/2015JA021138

King, J. H., & Papitashvili, N. E. (2005, Feb). Solar wind spatial scales in and comparisons of hourly Wind and ACE plasma and magnetic field data. *Journal of Geophysical Research (Space Physics)*, *110*(A2), A02104. doi: 10.1029/2004JA010649

Koskinen, H. E. J., & Huttunen, K. E. J. (2006, Jun). Geoeffectivity of Coronal Mass Ejections. *Space Science Reviews*, *124*(1-4), 169-181. doi: 10.1007/s11214-006-9103-0

Koval, A., & Szabo, A. (2010, Dec). Multispacecraft observations of interplanetary shock shapes on the scales of the Earth's magnetosphere. *Journal of Geophysical Research (Space Physics)*, *115*(A12), A12105. doi: 10.1029/2010JA015373

Lepping, R. P., Berdichevsky, D. B., Wu, C. C., Szabo, A., Narock, T., Mariani, F., ... Quivers, A. J. (2006, Mar). A summary of WIND magnetic clouds for years 1995-2003: model-fitted parameters, associated errors and classifications. *Annales Geophysicae*, *24*(1), 215-245. doi: 10.5194/angeo-24-215-2006

Liu, Y., Richardson, J. D., Belcher, J. W., Kasper, J. C., & Skoug, R. M. (2006, Sep). Plasma depletion and mirror waves ahead of interplanetary coronal mass ejections. *Journal of Geophysical Research (Space Physics)*, *111*(A9), A09108. doi: 10.1029/2006JA011723

Lugaz, N., Farrugia, C. J., Huang, C. L., & Spence, H. E. (2015, Jun). Extreme geomagnetic disturbances due to shocks within CMEs. *Geophysical Research Letters*, *42*(12), 4694-4701. doi: 10.1002/2015GL064530

Lugaz, N., Farrugia, C. J., Winslow, R. M., Al-Haddad, N., Galvin, A. B., Nieves-Chinchilla, T., ... Janvier, M. (2018, Sep). On the Spatial Coherence of Magnetic Ejecta: Measurements of Coronal Mass Ejections by Multiple Spacecraft Longitudinally Separated by 0.01 au. *The Astrophysical Journal Letters*, *864*(1), L7. doi: 10.3847/2041-8213/aad9f4

Lugaz, N., Farrugia, C. J., Winslow, R. M., Al-Haddad, N., Kilpua, E. K. J., & Riley, P. (2016, Nov). Factors affecting the geoeffectiveness of shocks and sheaths at 1 AU. *Journal of Geophysical Research (Space Physics)*, *121*(11), 10,861-10,879. doi: 10.1002/2016JA023100

Lugaz, N., Winslow, R. M., & Farrugia, C. J. (2020, Jan). Evolution of a long-duration coronal mass ejection and its sheath region between mercury and earth on 9–14 july 2013. *Journal of Geophysical Research: Space Physics*, *125*(1), e2019JA027213. doi: 10.1029/2019JA027213

Manchester, I., W. B., Gombosi, T. I., De Zeeuw, D. L., Sokolov, I. V., Roussev, I. I., Powell, K. G., ... Zurbuchen, T. H. (2005, Apr). Coronal Mass Ejection Shock and Sheath Structures Relevant to Particle Acceleration. *The Astrophysical Journal*, *622*(2), 1225-1239. doi: 10.1086/427768

Matthaeus, W. H., Dasso, S., Weygand, J. M., Milano, L. J., Smith, C. W., & Kivelson, M. G. (2005, Dec). Spatial Correlation of Solar-Wind Turbulence from Two-Point

Measurements. *Physical Review Letters*, *95*(23), 231101. doi: 10.1103/PhysRevLett.95.231101

Merka, J., Szabo, A., Slavin, J. A., & Peredo, M. (2005, Apr). Three-dimensional position and shape of the bow shock and their variation with upstream Mach numbers and interplanetary magnetic field orientation. *Journal of Geophysical Research (Space Physics)*, *110*(A4), A04202. doi: 10.1029/2004JA010944

Moissard, C., Fontaine, D., & Savoini, P. (2019, Nov). A Study of Fluctuations in Magnetic Cloud-Driven Sheaths. *Journal of Geophysical Research (Space Physics)*, *124*(11), 8208-8226. doi: 10.1029/2019JA026952

Myllys, M., Kilpua, E. K. J., Lavraud, B., & Pulkkinen, T. I. (2016, May). Solar wind-magnetosphere coupling efficiency during ejecta and sheath-driven geomagnetic storms. *Journal of Geophysical Research (Space Physics)*, *121*(5), 4378-4396. doi: 10.1002/2016JA022407

Nakagawa, T., Nishida, A., & Saito, T. (1989, Sep). Planar magnetic structures in the solar wind. *Journal of Geophysical Research*, *94*(A9), 11761-11775. doi: 10.1029/JA094iA09p11761

Neugebauer, M., Clay, D. R., & Gosling, J. T. (1993, Jun). The origins of planar magnetic structures in the solar wind. *Journal of Geophysical Research*, *98*(A6), 9383-9390. doi: 10.1029/93JA00216

Nieves-Chinchilla, T., Vourlidas, A., Raymond, J. C., Linton, M. G., Al-haddad, N., Savani, N. P., ... Hidalgo, M. A. (2018, Feb). Understanding the Internal Magnetic Field Configurations of ICMEs Using More than 20 Years of Wind Observations. *Solar Physics*, *293*(2), 25. doi: 10.1007/s11207-018-1247-z

Ogilvie, K. W., Coplan, M. A., Roberts, D. A., & Ipavich, F. (2007, Aug). Solar wind structure suggested by bimodal correlations of solar wind speed and density between the spacecraft SOHO and Wind. *Journal of Geophysical Research (Space Physics)*, *112*(A8), A08104. doi: 10.1029/2007JA012248

Olkin, I., & Pratt, J. W. (1958, Mar). Unbiased estimation of certain correlation coefficients. *The Annals of Mathematical Statistics*, *29*(1), 201–211. doi: 10.1214/aoms/1177706717

Owens, M. J., Cargill, P. J., Pagel, C., Siscoe, G. L., & Crooker, N. U. (2005, Jan). Characteristic magnetic field and speed properties of interplanetary coronal mass ejections and their sheath regions. *Journal of Geophysical Research (Space Physics)*, *110*(A1), A01105. doi: 10.1029/2004JA010814

Owens, M. J., Lockwood, M., & Barnard, L. A. (2017, Jun). Coronal mass ejections are not coherent magnetohydrodynamic structures. *Scientific Reports*, *7*, 4152. doi: 10.1038/s41598-017-04546-3

Palmerio, E., Kilpua, E. K. J., & Savani, N. P. (2016, Feb). Planar magnetic structures in coronal mass ejection-driven sheath regions. *Annales Geophysicae*, *34*(2), 313-322. doi: 10.5194/angeo-34-313-2016

Pomoell, J., & Poedts, S. (2018, Jun). EUHFORIA: European heliospheric forecasting information asset. *Journal of Space Weather and Space Climate*, *8*, A35. doi: 10.1051/swsc/2018020

Richardson, J. D., & Paularena, K. I. (2001, Jan). Plasma and magnetic field correlations in the solar wind. *Journal of Geophysical Research*, *106*(A1), 239-252. doi: 10.1029/2000JA000071

Riley, P., & Crooker, N. U. (2004, Jan). Kinematic Treatment of Coronal Mass Ejection Evolution in the Solar Wind. *The Astrophysical Journal*, *600*(2), 1035-1042. doi: 10.1086/379974

Salman, T. M., Winslow, R. M., & Lugaz, N. (2020, Jan). Radial evolution of coronal mass ejections between MESSENGER, Venus Express, STEREO, and L1: Catalog and Analysis. *Journal of Geophysical Research: Space Physics*, *125*(1), e2019JA027084. doi: 10.1029/2019JA027084

Samsonov, A. A., Sibeck, D. G., & Imber, J. (2007, Dec). MHD simulation for the interaction of an interplanetary shock with the Earth's magnetosphere. *Journal of Geophysical*

Research (Space Physics), *112*(A12), A12220. doi: 10.1029/2007JA012627

Shue, J. H., Song, P., Russell, C. T., Steinberg, J. T., Chao, J. K., Zastenker, G., ... Kawano, H. (1998, Aug). Magnetopause location under extreme solar wind conditions. *Journal of Geophysical Research*, *103*(A8), 17691-17700. doi: 10.1029/98JA01103

Siscoe, G., MacNeice, P. J., & Odstrcil, D. (2007, Apr). East-west asymmetry in coronal mass ejection geoeffectiveness. *Space Weather*, *5*(4), S04002. doi: 10.1029/2006SW000286

Siscoe, G., & Odstrcil, D. (2008, Dec). Ways in which ICME sheaths differ from magnetosheaths. *J. Geophys. Res.-Space*, *113*, A00B07. doi: 10.1029/2008JA013142

Tsurutani, B. T., Gonzalez, W. D., Tang, F., Akasofu, S. I., & Smith, E. J. (1988, Aug). Origin of interplanetary southward magnetic fields responsible for major magnetic storms near solar maximum (1978-1979). *Journal of Geophysical Research*, *93*(A8), 8519-8531. doi: 10.1029/JA093iA08p08519

Tsurutani, B. T., Wu, S. T., Zhang, T. X., & Dryer, M. (2003, Dec). Coronal Mass Ejection (CME)-induced shock formation, propagation and some temporally and spatially developing shock parameters relevant to particle energization. *Astronomy and Astrophysics*, *412*, 293-304. doi: 10.1051/0004-6361:20031413

Welch, B. L. (1938). The significance of the difference between two means when the population variances are unequal. *Biometrika*, *29*(3/4), 350–362. doi: 10.2307/2332010

Wicks, R. T., Chapman, S. C., & Dendy, R. O. (2009, Jan). Spatial Correlation of Solar Wind Fluctuations and Their Solar Cycle Dependence. *The Astrophysical Journal*, *690*(1), 734-742. doi: 10.1088/0004-637X/690/1/734

Wilson, R. M. (1987, Mar). Geomagnetic response to magnetic clouds. *Planetary and Space Science*, *35*(3), 329-335. doi: 10.1016/0032-0633(87)90159-0

Yermolaev, Y. I., Nikolaeva, N. S., Lodkina, I. G., & Yermolaev, M. Y. (2012, May). Geoeffectiveness and efficiency of CIR, sheath, and ICME in generation of magnetic storms. *Journal of Geophysical Research (Space Physics)*, *117*, A00L07. doi: 10.1029/2011JA017139

Zhang, G., & Burlaga, L. F. (1988, Apr). Magnetic clouds, geomagnetic disturbances, and cosmic ray decreases. *Journal of Geophysical Research*, *93*(A4), 2511-2518. doi: 10.1029/JA093iA04p02511

Zhang, J., Richardson, I. G., Webb, D. F., Gopalswamy, N., Huttunen, E., Kasper, J. C., ... Zhukov, A. N. (2007, Oct). Solar and interplanetary sources of major geomagnetic storms (Dst <= -100 nT) during 1996-2005. *Journal of Geophysical Research (Space Physics)*, *112*(A10), A10102. doi: 10.1029/2007JA012321

Zhao, X. H., Feng, X. S., Feng, H. Q., & Li, Z. (2017, Nov). Correlation between Angular Widths of CMEs and Characteristics of Their Source Regions. *The Astrophysical Journal*, *849*(2), 79. doi: 10.3847/1538-4357/aa8e49

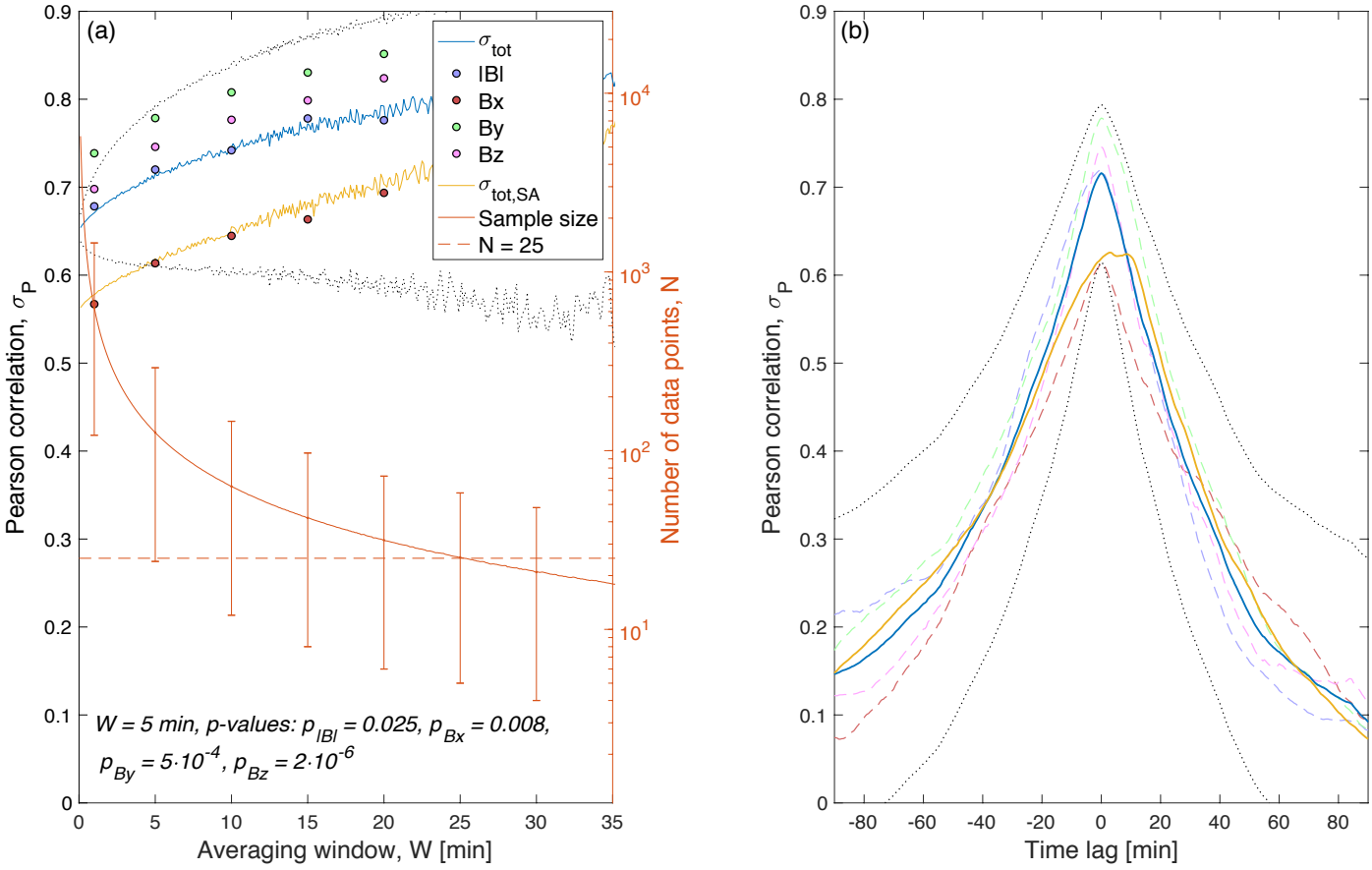

Figure 1. Average Pearson correlation (σ_P) of all studied events as a function of (a) the length of data averaging window (W), and (b) time lag of *Wind* data with respect to maximum σ_{tot} achieved with ACE data. (a) The total Pearson correlation (σ_{tot}; blue curve), i.e., the average of the correlations of the magnetic field magnitude and components (Olkin & Pratt, 1958), is plotted with the lower and upper bounds for a 95% confidence interval (black dots). Yellow curve shows the total correlation when the beginning of the sheath is aligned. P-values of magnetic field magnitude and components are the averages of p-values of studied events for 5 min averaging window. The average sample size (red curve) has its axis on the right and its error bars show the minimum and maximum sample sizes for a given W. (b) $W = 5$ min is used, and color codes are the same as in panel (a).

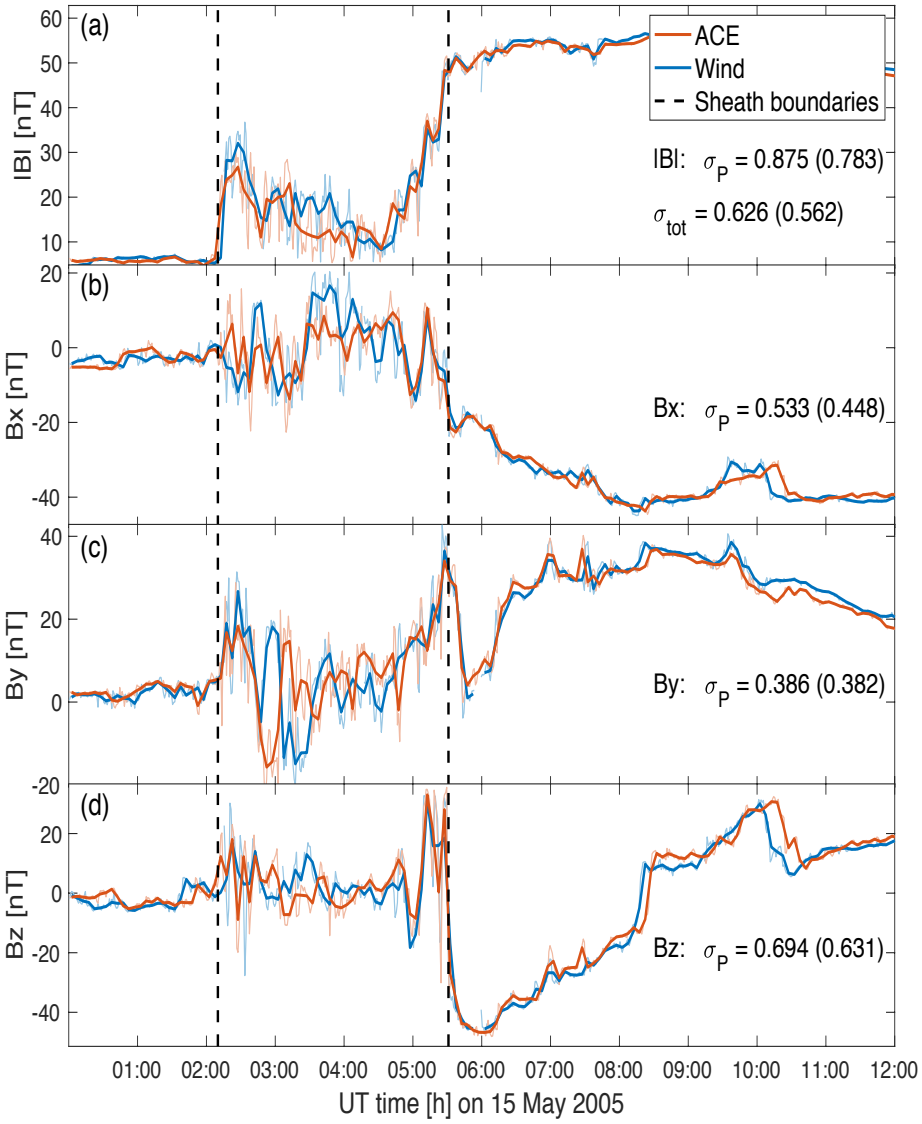

Figure 2. Magnetic field (a) magnitude, and (b-d) components in the GSE coordinates measured by ACE (orange) and *Wind* (blue; time-shifted) spacecraft for the ICME-driven sheath region observed on 15 May 2005. The non-radial spacecraft separation during the event was 0.0036 AU. Data is averaged using 5 min window length, and, for comparison, also 1 min averaging (shaded) is shown. Black dashed vertical lines indicates the beginning and ending of the sheath within which the Pearson correlation coefficients are computed. Coefficients in brackets are for 1 min averaging and panel (a) also gives the value of σ_{tot} of this event according to Eq. 1.

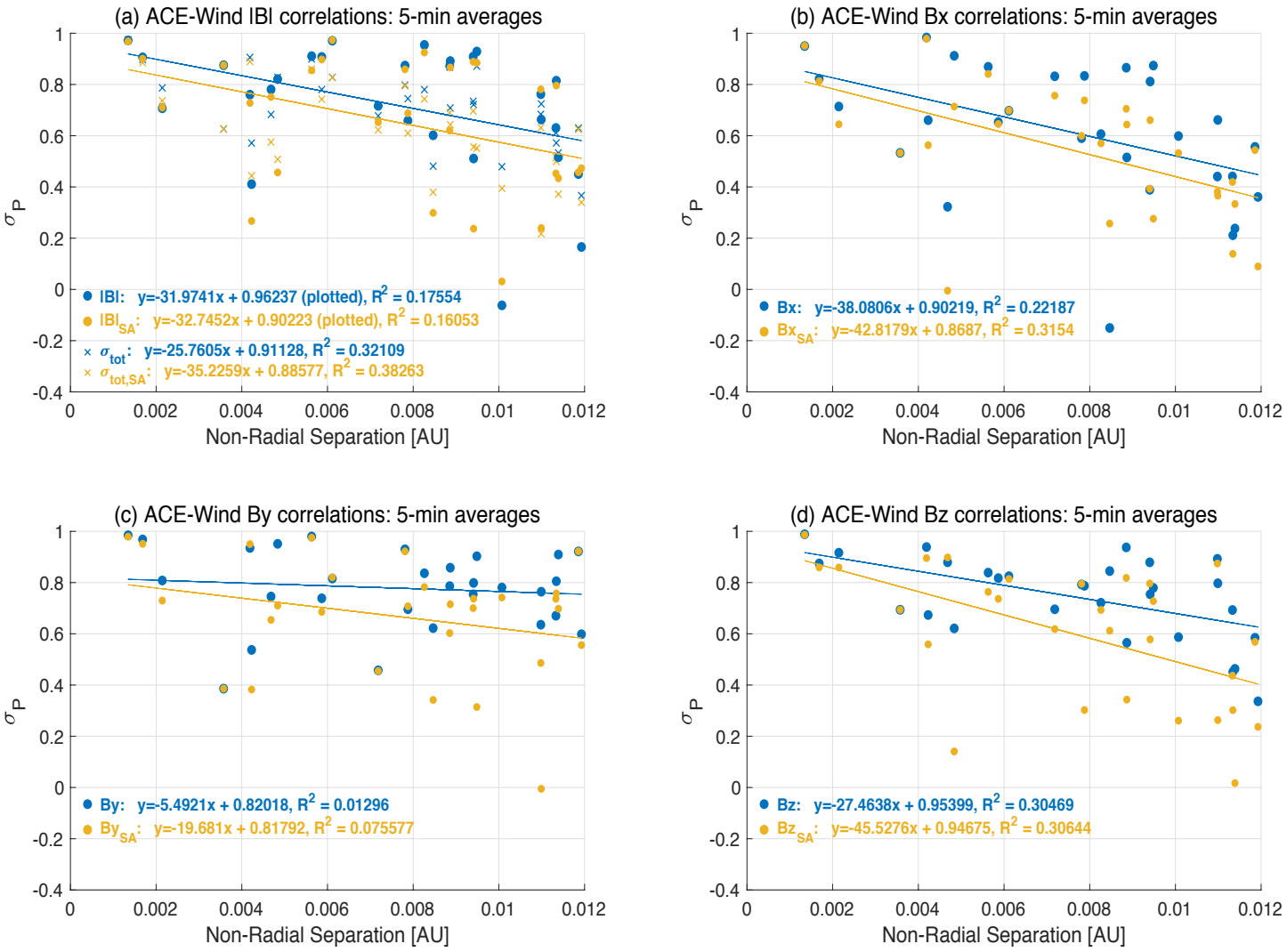

Figure 3. Pearson correlation coefficients of magnetic field (a) magnitude, and (b-d) components in the GSE coordinates measured by ACE and *Wind* as a function of non-radial separation of the spacecraft. Panels also plot linear evaluation and show the corresponding equation with R^2 values. Correlations and fits are also shown for *Wind* data shift according to shock alignment (yellow). The values and the equation of linear fitting with R^2 values of σ_{tot} (crosses) are given in panel (a). The data used to create this figure is available and given in the supplementary that also lists the studied ICME sheaths.

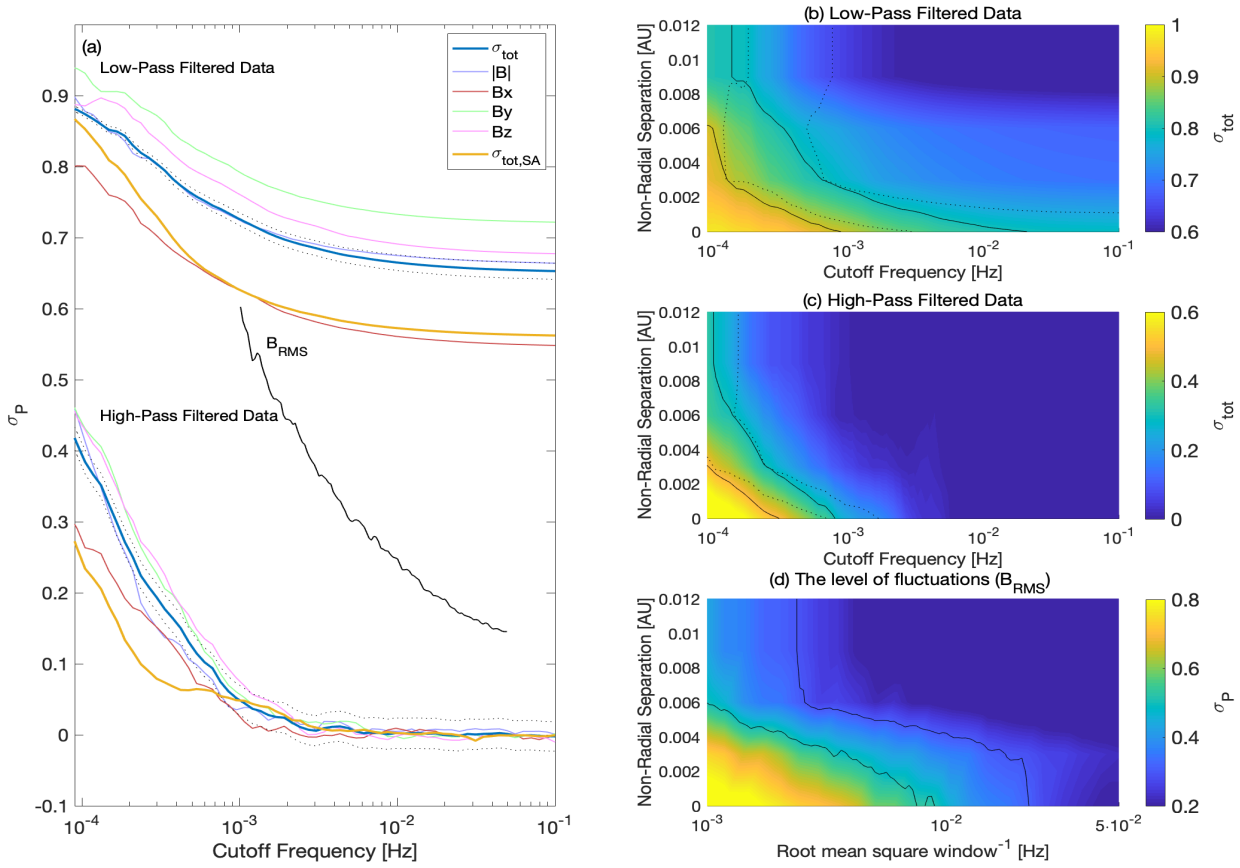

Figure 4. Correlation as a function of frequency filtered magnetic field data. (a) Average correlation of all studied events for both low- and high-pass filtered data, and for the level of fluctuations (B_{RMS}) as a function of cutoff frequency. The total Pearson correlation (blue curve) is plotted with the lower and upper bounds for a 95% confidence interval (black dots). (b) Total correlation as a function of cutoff frequency and non-radial separation for low-pass filtered data. Solid contours mark $\sigma_{tot} = 0.8$ and $\sigma_{tot} = 0.9$. For comparison, dotted contours give the corresponding interfaces for B_y. (c) Total correlation as a function of cutoff frequency and non-radial separation for high-pass filtered data. Solid contours mark $\sigma_{tot} = 0.3$ and $\sigma_{tot} = 0.5$ and dotted contours are for B_y. (d) Correlation as a function of the inverse of root-mean-square window and non-radial separation for the level of fluctuations. Solid contours mark $\sigma_P = 0.3$ and $\sigma_P = 0.5$. Note different color scales in panels (b), (c) and (d).

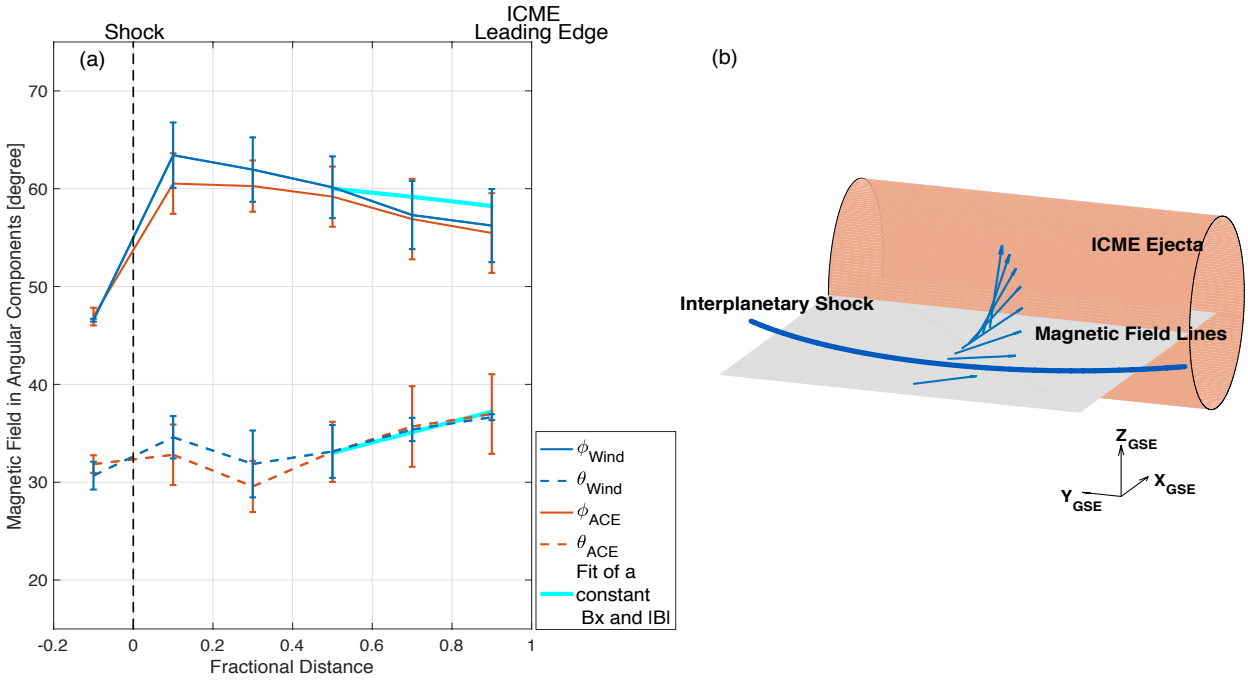

Figure 5. (a) Absolute averages of the magnetic field vector in GSE angular coordinates (ϕ - azimuth, θ - elevation) as a function of fractional distance (zero indicating the shock and one the leading edge of the ICME) in bins of 0.2. Here the absolute θ and ϕ angles range from 0 to 90°. $\theta = 0°$ ($\theta = 90°$) corresponds to vectors in the x-y plane (normal to the plane). $\phi = 0°$ ($\phi = 90°$) corresponds to vectors pointing in the x or -x (y or -y) direction when projected onto the x-y plane. Angles for preceding solar wind are computed from two hour intervals before the shock. Error bars indicate the standard deviation. Cyan curves show the fittings for a decreasing ϕ when B_x and $|B|$ are kept constant from ($\phi = 60°$, $\theta = 33°$) to a limiting observational boundary point (56°, 37°). The limiting boundary point defines the boundary over which the fitting is not extended. Fittings have final values of $\phi = 58°$ and $\theta = 37°$. (b) Illustration of field line draping for decreasing ϕ towards the back of the sheath with constant B_x and $|B|$. From the shock to ejecta, the field vectors have increasing z-component, decreasing y-component and constant x-component.

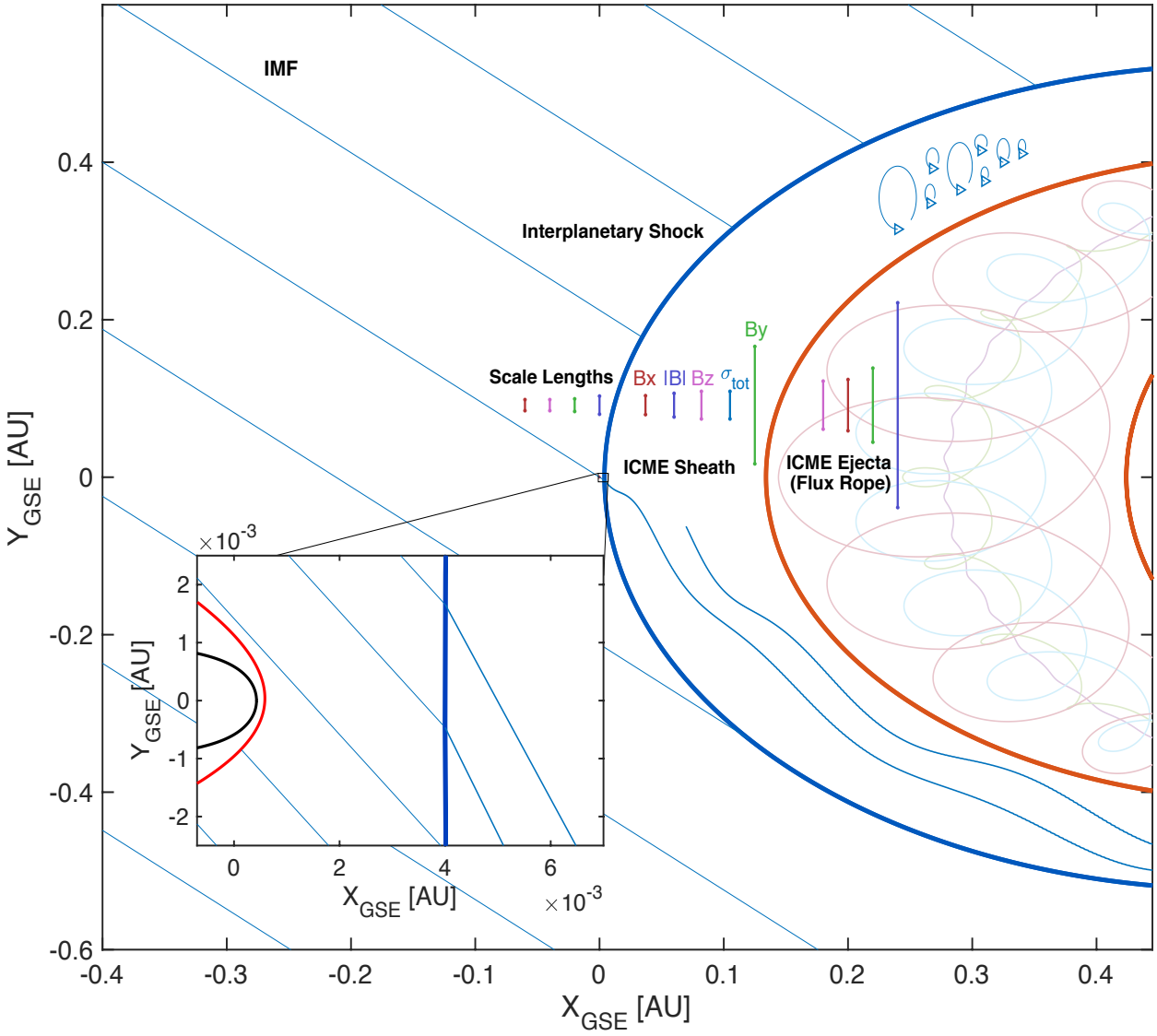

Figure 6. Sketch of an ICME complex in Earth-centered interplanetary space in the ecliptic plane. The ICME sheath is preceded by an interplanetary shock (dark blue curve) and driven by ICME ejecta, bounded by orange curves, within which there is a flux rope illustrated with an exaggerated twist. The ICME complex is modeled as arcs of a circle by taking the average angular width of the ICME ejecta given by Zhao et al. (2017) and the average radial width reported by Kilpua, Koskinen, and Pulkkinen (2017) for the sheath. Blue lines show interplanetary magnetic field (IMF) that has 45° Parker spiral angle at the Earth's distance from the Sun. The sheath is occupied by magnetic fluctuations and the field lines drape around the ICME ejecta. Also, turbulent progress of the fluctuations is exemplified by the eddies within the sheath. Scale lengths of the solar wind (Richardson & Paularena, 2001), ICME sheath (Table 1), and ICME ejecta (Lugaz et al., 2018) are illustrated in the y-direction. The near-Earth space is shown in the zoomed box where red and black curves indicate the bow shock and magnetopause boundaries that are estimated by using the models given by and Merka et al. (2005) and Shue et al. (1998), respectively, during nominal solar wind conditions.